Influence of potential vorticity generated by diabatic cooling over the Tibetan Plateau on the surface air temperature of Eastern China during Boreal Winter

Influence of Potential Vorticity Generated by Diabatic Cooling over the Tibetan Plateau on the Surface Air Temperature of Eastern China during Boreal Winter

CHEN SHENG,[a,c] BRIAN HOSKINS,[d,e] JOHN METHVEN,[d] GUOXIONG WU,[b,c] YIMIN LIU,[b,c] AND BIAN HE[b,c]

[a] *State Key Laboratory of Numerical Modeling for Atmospheric Sciences and Geophysical Fluid Dynamics (LASG), Institute of Atmospheric Physics, Chinese Academy of Sciences, Beijing, China*
[b] *Key Laboratory of Earth System Numerical Modeling and Application, Institute of Atmospheric Physics, Chinese Academy of Sciences, Beijing, China*
[c] *University of Chinese Academy of Sciences, Beijing, China*
[d] *Department of Meteorology, University of Reading, Reading, United Kingdom*
[e] *Grantham Institute for Climate Change, Imperial College, London, United Kingdom*

(Manuscript received 12 December 2024, in final form 11 March 2025, accepted 24 April 2025)

ABSTRACT: Using reanalysis and model data, this study investigates potential vorticity (PV) generated by diabatic cooling over the Tibetan Plateau (TP) and its associated climatic effects on adjacent regions. Results suggest that anomalous diabatic cooling over the TP exhibits a bottom-heavy vertical structure, which leads to the generated positive PV anomaly being confined within a shallow near-surface layer. The total PV generation anomaly within this layer is determined by the anomalous surface PV generation flux that is thermally driven by anomalous surface cooling. Further analysis revealed a significant interannual relationship linking stronger near-surface PV generation over the TP with anomalously warm winters in eastern China. The proposed mechanism involves PV generation by surface cooling, PV transport by katabatic flows, and an attendant weakened Siberian High. The surface cooling anomaly over the TP generates a positive PV anomaly within the near-surface layer, while simultaneously induces a form of anomalous katabatic flow down the slopes of the TP. This anomalous katabatic flow transports positive PV within the near-surface layer into the region of the Siberian High, increasing the local positive PV anomaly and weakening the Siberian High. A weaker Siberian High is associated with weaker winter monsoon flow and anomalous southerlies, leading to a warm surface air temperature anomaly over eastern China. The validity of the proposed mechanism was corroborated by numerical modeling. Relative to the well-studied winter blocking effect of the TP, this study offers and emphasizes new aspects of the TP's climatic effects driven by its wintertime thermal conditions.

SIGNIFICANCE STATEMENT: The purpose of this study was to better understand the thermal effects of the Tibetan Plateau on surrounding regions during winter. We found that wintertime surface cooling over the Tibetan Plateau generates positive potential vorticity and induces downslope katabatic flows within the near-surface layer. The generated potential vorticity transported by these katabatic flows exerts substantial climatic impacts on surrounding areas. This result importantly reveals that the wintertime thermal effects of the Tibetan Plateau could be critical in driving the climate of eastern China. In addition to consideration of the blocking effect of the Tibetan Plateau, our results suggest that greater attention should be given to its thermal effects during wintertime.

KEYWORDS: Potential vorticity; Climate; Diabatic heating; Katabatic winds; Temperature

1. Introduction

Potential vorticity (PV), an important physical variable that couples the atmospheric dynamic and thermodynamic information, was introduced by the pioneers Rossby (1940) and Ertel (1942), and its use in meteorology and atmospheric dynamics was comprehensively reviewed by Hoskins et al. (1985). Many studies have investigated how PV redistribution in the atmosphere can impact midlatitude synoptic developments (e.g., Hoskins 1997), rainstorms and cold events (e.g., Wu et al. 1995; Wu and Cai 1997; Zhao and Ding 2009), Rossby wave breaking (Folkins and Appenzeller 1996; Ryoo et al. 2013; Bowley et al. 2019), ozone distribution (Danielsen 1968; Allaart et al. 1993; Folkins and Appenzeller 1996; Sandhya et al. 2015), and many other aspects of the atmospheric general circulation. PV redistribution within the troposphere is often the primary focus of such studies; however, it has been suggested that surface PV generation, especially over the Tibetan Plateau (TP), plays a crucial role in the variability of the general circulation (e.g., Hoskins 1997; Ma et al. 2019; Sheng et al. 2021; Xie et al. 2023; Wu et al. 2024).

The TP plays a crucial role in shaping both regional and global climatic anomalies (e.g., Flohn 1957; Yeh et al. 1957; Hahn and Manabe 1975; Wu et al. 1997, 2007, 2012, 2015, 2018; Chen et al. 1999; Liu 1999; Son et al. 2019). Recently, Liu et al. (2020) and Huang et al. (2023) reviewed the climatic effects of the TP. During summertime, the TP acts as a notable heat source that greatly influences the formation of the

Denotes content that is immediately available upon publication as open access.

Corresponding author: Chen Sheng, shengchen@lasg.iap.ac.cn

DOI: 10.1175/JCLI-D-24-0732.1

Asian summer monsoon through a mechanism known as the TP sensible-heat-driven air pump (Wu et al. 1997, 2007; Wu and Zhang 1998; He et al. 2015, 2019). Beyond the adjacent regions of Asia, TP heating can trigger Rossby waves and alter zonal and meridional vertical circulation cells, leading to notable anomalies of rainfall and temperature over the North Atlantic, Mediterranean Sea, and Indian Ocean (Lu et al. 2018; Nan et al. 2019; Yang et al. 2020; Zhao et al. 2019; Zhou et al. 2009), the Pacific Ocean (Sun et al. 2019), and the pan-Arctic areas of Europe and America (Liu et al. 2020; Lu et al. 2018; Zhao et al. 2019). Current understanding regarding the wintertime climatic influence of the TP still centers on its blocking effect, whereby westerly winds are deflected by the high-elevation topography of the TP (Yeh et al. 1957; Huang et al. 2023). The westerly winds are split by the TP, flowing to its north and south before converging to its east and forming the world's strongest westerly jet over East Asia, which affects the weather and climate patterns of the wider Asia–Pacific region (Yang et al. 2002; Huang et al. 2023). The few studies that have focused on the thermal forcing of the TP in wintertime suggested that thermal anomalies could influence the climate over East Asia and over North America through teleconnections (e.g., Yu et al. 2011a,b; Lin and Wu 2011, 2012). Overall, relative to the well-studied summer thermal effects of the TP, few studies have examined its climatic effects in winter, particularly its thermal effects.

The surface air temperature (SAT) anomaly in eastern China could lead to the disasters of persistent rain, snow, and ice storms, greatly influencing the transportation and energy supply (Ding et al. 2008). The objectives of this study were to investigate near-surface PV generation driven by the diabatic cooling anomaly over the TP during boreal winter and its remote impact on the SAT in eastern China, and to elucidate the possible mechanism linking the two regions using reanalysis data and numerical modeling. The remainder of this paper is organized as follows. Section 2 documents the data, diagnostics, and model used in the study. Section 3 presents the definition of near-surface PV generation over the TP. Section 4 examines the impact of near-surface PV generation over the TP on eastern China SAT during boreal winter and proposes the possible mechanism. Finally, a summary and a discussion are presented in section 5.

2. Data, model, and diagnostics

a. Reanalysis data

The reanalysis data used in this study are from the Modern-Era Retrospective Analysis for Research and Applications, version 2 (MERRA-2) (Rienecker et al. 2011; Gelaro et al. 2017), with a horizontal resolution of 1.25° × 1.25° for the period 1980–2022. Monthly data archived on hybrid σ–p model levels (i.e., η coordinates), which transition smoothly from a terrain-following coordinate near the surface to fixed pressure levels in the upper atmosphere, include three-dimensional winds and air temperature. Table 1 shows the model levels used in this study and the corresponding pressure increments relative to the TP-averaged surface pressure that is 650 hPa in the winter climate mean. Monthly single-level data used in this study include 2-m temperature (SAT), 10-m zonal and meridional winds, surface pressure, and sea level pressure (SLP). High-frequency data with a 3-hourly interval archived at the hybrid σ–p model levels are adopted to calculate the diabatic heating rate, etc., which involve the product of multiple variables.

TABLE 1. Model levels used in this study and the corresponding pressure increments relative to the TP-averaged surface pressure of 650 hPa.

Model level	Reduction in pressure relative to surface pressure (hPa)	Model level	Reduction in pressure relative to surface pressure (hPa)
72	5	60	97
71	13	59	109
70	21	58	121
69	28	57	134
68	36	56	147
67	43	55	160
66	51	54	176
65	58	53	195
64	66	52	215
63	73	51	235
62	81	50	255
61	88	49	276

The monthly TN10p, which is a measurement of the frequency of extreme cold events and is directly provided by MERRA-2, is also used. The TN10p in MERRA-2 is defined as the percentage of time when daily minimum 2-m temperature is less than the 10th percentile. The percentile computed based on daily temperature was calculated using a running window of ±7 days centered on each day of the year for the climatology period of 1981–2010.

The Niño-3.4 index, which is defined by the averaged SST anomalies over 5°S–5°N and 170°–120°W, is obtained from the National Oceanic and Atmospheric Administration, Physical Sciences Laboratory (https://psl.noaa.gov/data/climateindices/list/).

In this study, boreal winter refers to the time average over December–February. The "TP averaged" refers to spatial averaging over the TP with elevation above 2000 m unless stated otherwise. The "***" ("**"/"*") indicates a significance level exceeding 0.01 (0.05/0.1) unless otherwise specified.

b. Climate ensemble simulations

To support the hypothesized mechanisms developed through the diagnosis of MERRA-2 data, we utilized the Community Earth System Model (version 1) Large Ensemble (CESM1-LE) with 40 members. All CESM1-LE members only differ in their initial conditions but have the same external forcing. Following the CMIP5 design protocol, the CESM1-LE applied historical forcing from 1920 to 2005 and representative concentration pathway 8.5 from 2006 to 2100. In this study, only the historical simulation for the period 1920–2005 is used. The diabatic heating rate in CESM1-LE is obtained by summing the longwave heating rate, solar heating rate, vertical diffusion, and moist processes. All variables in CESM1-LE used in this study are archived at the

hybrid σ–p model level. The time frequency is monthly, and the horizontal resolution is 1.25° × 0.94° (longitude × latitude). More details regarding the CESM1-LE experimental design can be found in Kay et al. (2015).

c. Diagnostics

The PV, PV per unit volume (i.e., PV substance) and its budget equation (Hoskins 1991; Bretherton and Schär 1993; Sheng et al. 2022a, 2023) are, respectively,

$$\mathrm{PV} = \alpha \boldsymbol{\zeta}_a \cdot \nabla\theta, \tag{1}$$

$$W = \boldsymbol{\zeta}_a \cdot \nabla\theta, \tag{2}$$

and

$$\frac{\partial W}{\partial t} = -\nabla \cdot (\mathbf{V}W - \mathbf{F} \times \nabla\theta - \boldsymbol{\zeta}_a \dot{\theta}). \tag{3}$$

Here, $\mathbf{V}$ is the three-dimensional wind vector; $\alpha = 1/\rho$ is the specific volume, and ρ is the air density; $\boldsymbol{\zeta}_a$ is the three-dimensional absolute vorticity vector; θ is the potential temperature; and $\dot{\theta}$ is the diabatic heating rate. Equation (3) suggests the change in PV substance is made up of a term due to the advection, a term due to the friction, and a generation term associated with diabatic heating.

Since heating $\dot{\theta}$ is important to drive large-scale circulations, we start with the generation term:

$$\left(\frac{\partial W}{\partial t}\right)_G = -\nabla \cdot (-\boldsymbol{\zeta}_a \dot{\theta}). \tag{4}$$

The subscript G represents PV generation. With reference to Liu et al. (2023), considering an enclosed spherical atmospheric layer δ bounded by an upper boundary Σ and Earth's surface S, and using the Gauss divergence theorem for Eq. (4), we can have the total PV generation within δ layer as follows:

$$\iiint_{\delta} \left(\frac{\partial W}{\partial t}\right)_G dV = \iint [G_C(S) - G_C(\Sigma)] dx dy. \tag{5}$$

Here, dV is the volume element. In Eq. (5), G_C, given by

$$G_C = -\dot{\theta}\left(f + \frac{\partial v}{\partial x} - \frac{\partial u}{\partial y}\right), \tag{6}$$

is introduced as the PV generation flux related to the diabatic cooling because of the minus sign in front of $\dot{\theta}$. A positive (negative) generation flux G_C at a certain level represents a positive (negative) contribution to the total PV of the atmosphere above this level. Equation (5) suggests that the total PV generation within δ layer is determined by the vertical difference, in other words, the vertical profile, of the generation flux G_C between Earth's surface S and the upper boundary Σ.

The diabatic heating rate is formulated for the hybrid σ–p model level as

$$\dot{\theta} \equiv \frac{D\theta}{Dt} = \frac{\partial\theta}{\partial t} + \left(u\frac{\partial\theta}{\partial x} + v\frac{\partial\theta}{\partial y}\right)_\eta + \dot{\eta}\frac{\partial p}{\partial \eta}\frac{\partial\theta}{\partial p}, \tag{7}$$

in which $\dot{\eta}$ is the vertical velocity at the hybrid σ–p model level. Similarly, the Lagrangian change of pressure is given by $\omega \equiv Dp/Dt = \partial p/\partial t + [u(\partial p/\partial x) + v(\partial p/\partial y)]_\eta + \dot{\eta}(\partial p/\partial \eta)$. The subscript η indicates that the differential is taken on the hybrid σ–p model level. By solving $\dot{\eta}$ in ω and substituting it into Eq. (7), we have a form of diabatic heating rate that can be calculated directly by the variables provided in reanalysis data:

$$\dot{\theta} \equiv \frac{D\theta}{Dt} = \frac{\partial\theta}{\partial t} + \left(u\frac{\partial\theta}{\partial x} + v\frac{\partial\theta}{\partial y}\right)_\eta + \omega_\eta \frac{\partial\theta}{\partial p}, \tag{8}$$

in which $\omega_\eta = \omega - \partial p/\partial t - [u(\partial p/\partial x) + v(\partial p/\partial y)]_\eta$ indicates the vertical velocity at the hybrid σ–p model level adjusted based on the vertical coordinate transformation (Xie et al. 2022). The deduction is similar with that in Xie et al. (2022) and Sheng et al. (2021). In this study, the PV, diabatic heating, and PV generation on the surface are referred to those calculated on the lowest model level (i.e., the 72nd level) unless stated otherwise.

3. Index of diabatic-cooling-generated PV within the near-surface layer over the TP

In this section, we introduce the index of PV generation within the near-surface layer over the TP due to diabatic cooling that is used in this paper.

The climatic mean of the surface $\dot{\theta}$ and a vertical profile of the TP-averaged $\dot{\theta}$ are shown in Figs. 1a and 1b, respectively. In wintertime, diabatic cooling over the TP is prominent on the surface (Fig. 1a) and vertically (Fig. 1b), suggesting that the TP is a cooling source during wintertime (Yeh et al. 1957; Liu et al. 2020). The vertical profile of TP-averaged $\dot{\theta}$ (Fig. 1b) exhibits a bottom-heavy vertical structure, indicating that substantial cooling occurs at the lower level, which resembles the structure of longwave radiative cooling (Wu et al. 2007; Xie et al. 2023). Figures 1c and 1d are the same as Figs. 1a and 1b, respectively, but show the results of regression onto the TP surface cooling index (blue line in Fig. 2c), which is defined as the normalized time series of the TP-averaged surface $-\dot{\theta}$. In terms of variability, the patterns associated with TP surface cooling (Figs. 1c,d) are very similar to those of their climatic mean (Figs. 1a,b). During the phase of anomalous TP surface cooling (positive TP surface cooling index), anomalous cooling signals are particularly evident (Fig. 1c) over western parts where the center of maximum variation in snow depth is located (Chen et al. 2020). The vertical profile of anomalous $\dot{\theta}$ (Fig. 1d) also exhibits a bottom-heavy vertical structure. The strongest anomalous cooling occurs on the surface, decays upward to the 61st model level, and then finally transitions to a more vertical distribution above (Fig. 1d). Notably, from the surface to the 61st model level, the thickness is only approximately 88 hPa (Table 1). This means that the TP cooling anomaly is concentrated primarily within a shallow near-surface layer. For convenience, the symbol δ_0 is used in the following to refer to the near-surface layer bounded by the surface and the 61st model level. During the phase of anomalous TP surface warming (negative TP surface cooling index), the horizontal pattern and the vertical structure (Figs. 1c,d) would have the opposite signs.

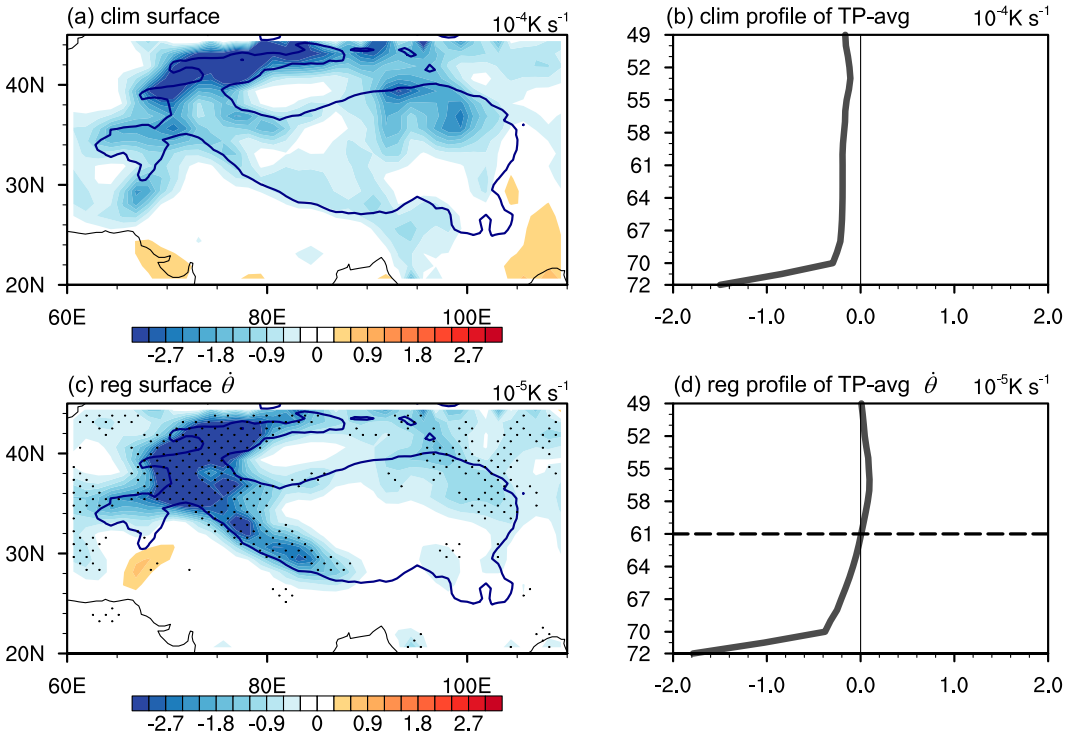

FIG. 1. (a) Climatic mean of surface $\dot{\theta}$ during boreal winter. (b) Climatic mean of the profile of the TP-averaged $\dot{\theta}$ during boreal winter (10^{-4} K s^{-1}). Labels on the vertical axis indicate the model-level number. (c),(d) As in (a) and (b), respectively, but showing regression onto the TP surface cooling index (10^{-5} K s^{-1}). The blue line in (a) and (c) denotes the boundary of the TP topography with an elevation of 2000 m. Areas exceeding a significance level of 0.1 are indicated by black dots.

According to Eqs. (5) and (6), because the PV generation flux G_C is related to $\dot{\theta}$, the horizontal and vertical patterns of $\dot{\theta}$ anomaly (Figs. 1c,d) are expected to influence G_C flux anomaly and the resultant PV generation.

By conducting regression onto the TP surface cooling index (blue line in Fig. 2c), Figs. 2a and 2b show the anomalous surface G_C flux and the vertical profile of the anomalous TP-averaged G_C flux, respectively. In the phase of anomalous TP surface cooling (positive TP surface cooling index), the TP exhibits a positive surface G_C flux anomaly (Fig. 2a). Following the shallow structure of anomalous $\dot{\theta}$ (Fig. 1d), the major G_C flux anomaly also shows a shallow structure that is confined primarily within the near-surface layer δ_0 (Fig. 2b). According to Eq. (5), the total PV generation within a layer is determined by the vertical difference in G_C flux. Here, for simplicity, if we select the 61st model level as the upper boundary Σ_0, where G_C (Σ_0) is close to zero, the total PV generation anomaly within the near-surface layer δ_0 could be expressed as follows:

$$\iiint_{\delta_0}\left(\frac{\partial W}{\partial t}\right)_G dV \simeq \iint G_C(S)dxdy. \tag{9}$$

Adjustment of the upper boundary would not overly influence Eq. (9) because G_C flux anomalies around the 61st model level are very close to each other (Fig. 2b). Equation (9) reveals the importance of the surface G_C flux for PV generation within the near-surface layer. It demonstrates that in the terms of variability, the total PV generation anomaly within the near-surface layer δ_0 is determined mostly by the surface G_C flux anomaly.

Figure 2c further shows the normalized time series of the TP-averaged surface G_C flux, hereafter, shortened to the raw G_C index (GCI, red line). The raw GCI is strongly correlated with the TP surface cooling index (blue line, Fig. 2c), yielding a correlation coefficient of 0.995 (passing the 0.01 significance level). This result indicates that the total variability in the surface G_C flux $G_C(S)$ is thermally driven by surface diabatic cooling. In other words, on the basis of Eq. (9), the surface diabatic cooling (heating) anomaly would generate a positive (negative) PV anomaly within the near-surface layer δ_0.

Overall, the results shown in Figs. 1 and 2 highlight two fundamental points. First, because of the bottom-heavy vertical structure of the anomalous $\dot{\theta}$, G_C flux anomaly also exhibits a bottom-heavy structure, which means that the total PV generation anomaly is concentrated within the shallow near-surface layer δ_0 [Eq. (9)]. Second, the surface G_C flux anomaly, which determines the total PV generation anomaly within the near-surface layer δ_0, is thermally driven by surface diabatic cooling (Fig. 2c).

To better elucidate the climate effect of the PV generation within the near-surface layer, we illustrate again the index we

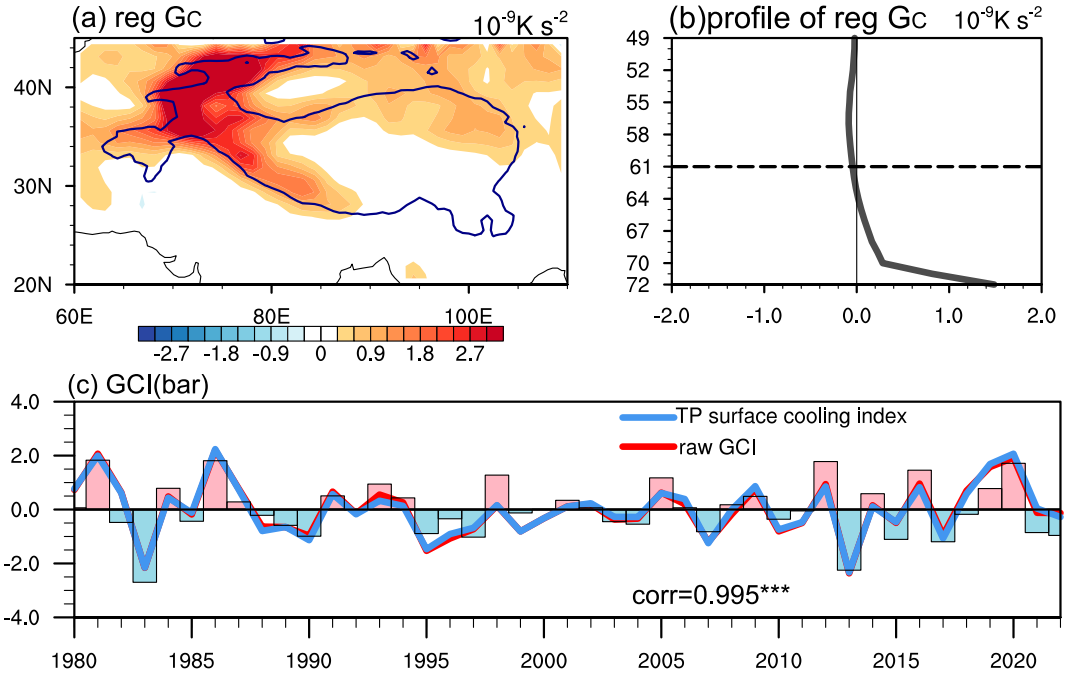

FIG. 2. (a) Regressed surface G_C on the TP surface cooling index (10^{-9} K s^{-2}). (b) Vertical profile of the regression of the TP-averaged G_C on the TP surface cooling index (10^{-9} K s^{-2}). Labels on the vertical axis indicate the model-level number. (c) Time series of the raw GCI (red line), the TP surface cooling index (blue line), and the GCI used in this study (bar). The blue line in (a) denotes the boundary of the TP topography with an elevation of 2000 m.

will use, GCI, which is defined as the normalized time series of the winter TP-averaged surface G_C flux. From the definition of G_C flux [Eq. (6)], whose average over the TP forms the GCI, it is important to note again that in the abbreviation GCI, the letter "G" refers to positive PV generation and the letter "C" refers to surface diabatic cooling. GCI for the period 1980–2022 is shown in Fig. 2c. On the basis of theoretical [Eq. (9)] and statistical analyses (Fig. 2c), this GCI can be regarded as a compound index, in which a positive value of the GCI indicates a positive PV generation anomaly within the near-surface layer δ_0 over the TP [Eq. (9)] and a surface diabatic cooling anomaly over the TP (Fig. 2c). Conversely, a negative value of the GCI indicates a negative PV generation anomaly within the near-surface layer δ_0 and a surface diabatic heating anomaly over the TP.

In this study, we focused on the interannual time scale; therefore, the actual GCI (bar, Fig. 2c) used for the following analysis was obtained by filtering out both the linear trend and the interdecadal variation over more than 9 years from the raw GCI. Additionally, the winter Niño-3.4 index was also linearly removed to exclude the ENSO signal.

4. Interannual impact of the GCI on winter surface air temperature in eastern China

a. *Relationship between the GCI and the winter SAT anomaly in eastern China*

Figure 3a presents the regressed winter SAT on the GCI. It is evident that positive values cover the entire area of eastern China and extend northward to the northern flank of the TP. There are also positive anomalies to the west of the TP but beyond the target region of interest in this study (will be discussed in section 5). Figure 3b shows the pattern of the regressed TN10p on the GCI, which resembles that shown in Fig. 3a but with opposite signs. Because the TN10p measures the frequency of extreme cold events, and warm SAT anomalies (Fig. 3a) tend to suppress extreme cold events, the reversed pattern of TN10p (Fig. 3b) is to be expected. These results suggest a notable positive relationship between the GCI and eastern China SAT in which the positive (negative) GCI favors a notably warm (cold) anomaly over eastern China during boreal winter.

Figure 4 presents scatter diagrams for the GCI and SAT (Fig. 4a) and for the GCI and TN10p (Fig. 4b) averaged within the box shown in Fig. 3b. Again, the positive relationship between the GCI and box-averaged SAT (Fig. 4a) and the negative relationship between the GCI and box-averaged TN10p (Fig. 4b) are very evident, with correlation coefficients of 0.55 and −0.45, respectively (both significant at the 0.01 level). Consistent with this, the number of years in the first and third quadrants of Fig. 4a is 32, whereas it is 11 in the second and fourth quadrants. In Fig. 4b, there are 31 years in the second and fourth quadrants and 12 years in the first and third quadrants. Their sign consistency rates are as high as 74% and 72% over the investigated 43 years (1980–2022), respectively. This high level of consistency suggests a strong likelihood that a positive (negative) GCI corresponds to an anomalous warm (cold) winter in eastern China, further confirming the

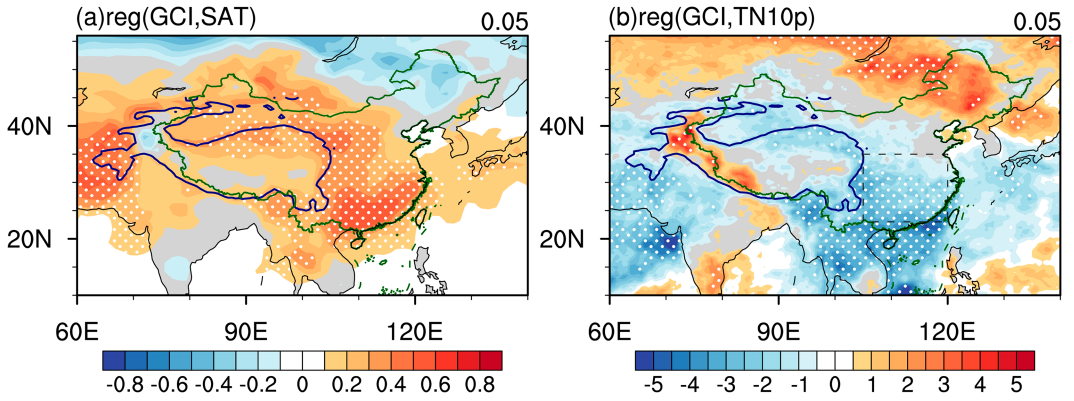

FIG. 3. (a) Regression of SAT on the GCI (°C). (b) As in (a), but for TN10p (%). Areas exceeding a significance level of 0.05 are indicated by white dots. The blue line denotes the boundary of the TP topography with an elevation of 2000 m. The area of China discussed below is shown by the rectangle with dashed lines in (b).

close relationship between the GCI and SAT condition over eastern China during boreal winter.

b. *Mechanism*

To investigate the mechanism by which the GCI influences eastern China SAT, a meridional cross section of the regressed PV (shading) and wind (vectors) averaged over 65°–105°E (the northern TP boundary shown as the black line in Fig. 5c) on the GCI is shown in Fig. 5a. Figure 5b shows the same as Fig. 5a but for the zonal cross section averaged over 27°–40°N (the eastern TP boundary shown as the black line in Fig. 5c). In the lower panels of Figs. 5a and 5b, the gray shading, black curve, and gray curve outline the heights of topography, the bottom model level, and the 61st model level, respectively. Intuitively, it is seen that the anomalous PV and atmospheric flow within the near-surface layer δ_0 (Figs. 5a,b) are occurring in the terrain-following layer between the gray and black curves shown in the lower panels of Figs. 5a and 5b. Corresponding to the positive GCI, the positive PV anomaly is concentrated within this shallow, terrain-following near-surface layer δ_0 (Figs. 5a,b). This is consistent with Eq. (9) and indicates that positive PV generation is primarily within the near-surface layer δ_0. Above the near-surface layer δ_0 is a deep, weak negative PV anomaly (Figs. 5a,b). The cooling over the TP behind the GCI anomaly increases the density of air in the near-surface layer, which then drains off the sides of the plateau (Figs. 5a,b) producing katabatic flows away from the plateau toward the east and north that can be locally strong. A katabatic flow is a downslope wind caused by the flow of a high-density air mass related to diabatic cooling, which is usually prominent on the slope of the near-surface layer (Parish and Bromwich 1991). These katabatic flows advect the positive PV (denoted schematically as blue vectors in Fig. 5c) from the plateau into the region of the

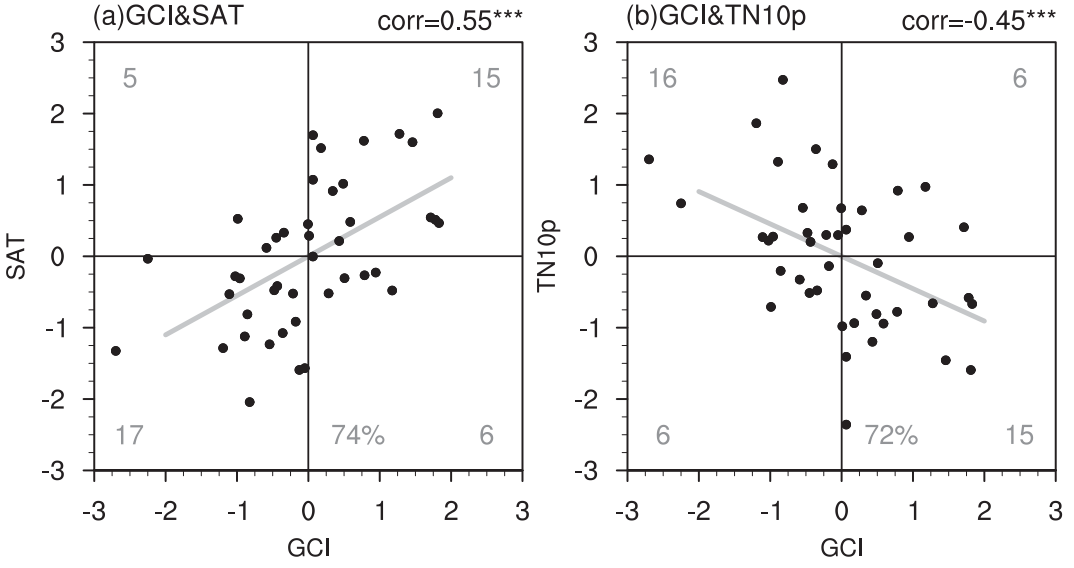

FIG. 4. Normalized scatter diagrams showing the GCI and the (a) SAT and (b) TN10p averaged in the box shown in Fig. 3b. The gray line indicates the slope calculated using the least squares fitting method.

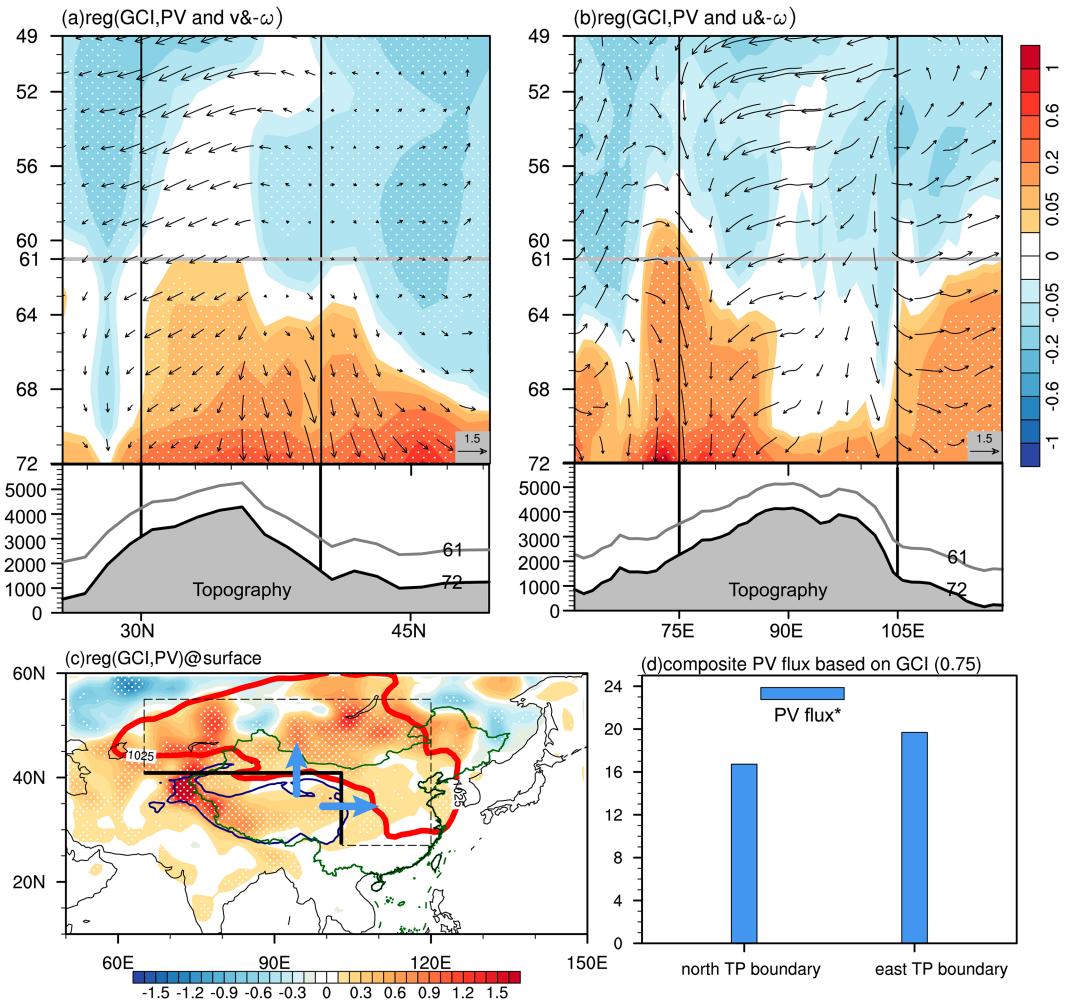

FIG. 5. (a) Cross section of the regression of 65°–105°E-averaged meridional circulation and PV on the GCI (10^{-1} PVU; 1 PVU = 10^{-6} K kg^{-1} m^2 s^{-1}). Labels on the vertical axis indicate the model-level number. Heights of the topography (shading), the lowest model level 72 (black line), and model level 61 (gray line) averaged over the same range are attached below. Values on the left axis in the attached figure indicate the height (m). (b) As in (a), but for 27°–40°N-averaged zonal circulation and PV. (c) Regressed near-surface PV on the GCI (10^{-1} PVU). The Siberian High is outlined by the red contour with a value of 1025 hPa. The PV fluxes are denoted schematically as blue vectors. (d) Composite difference in vertically averaged PV flux in the near-surface layer δ_0 crossing the northern (40°N, 65°–105°E) and eastern (27°–40°N; 105°E) TP boundaries between GCI > 0.75 and GCI < −0.75 (10^4 PVU m^2 s^{-1}). Areas exceeding a significance level of 0.05 in (a)–(c) are indicated by white dots. The blue line in (c) denotes the boundary of the TP topography with an elevation of 3000 m.

Siberian High (red contour in Fig. 5c). This is consistent with the results of the numerical experiment by Wu et al. (2007; their Fig. 4d) which suggests that the surface cooling of the TP plays an important role in driving the sinking motion and divergence of air into the surrounding area. We further calculated the composite difference in the near-surface layer-averaged PV flux (**V** PV) crossing the eastern and northern boundaries based on a threshold of ±0.75 standard deviations of the GCI. The outward PV flux from the TP (Fig. 5d) is significant at the 0.1 level. These PV fluxes across the northern and eastern boundaries within the near-surface layer would increase PV over the region of the Siberian High, as confirmed by the regressed surface PV on the GCI shown in Fig. 5c.

The Siberian High is characterized by high SLP accompanied by an anticyclonic circulation, and therefore the positive PV anomaly in Fig. 5c is expected to weaken the intensity of the Siberian High. This is because, in the Northern Hemisphere, a positive PV anomaly is associated with an anomalous cyclonic circulation. To further demonstrate the impact of the GCI on the Siberian High, with reference to both Panagiotopoulos et al. (2005) and Zhu et al. (2019), we defined the intensity of the Siberian High as the area-averaged SLP over the 40°–60°N, 80°–120°E. Figure 6a shows the scatter diagram for the GCI and Siberian High intensity. The negative relationship is very evident, in which 31 years in the second and fourth quadrants follow this negative relation. The correlation coefficient between

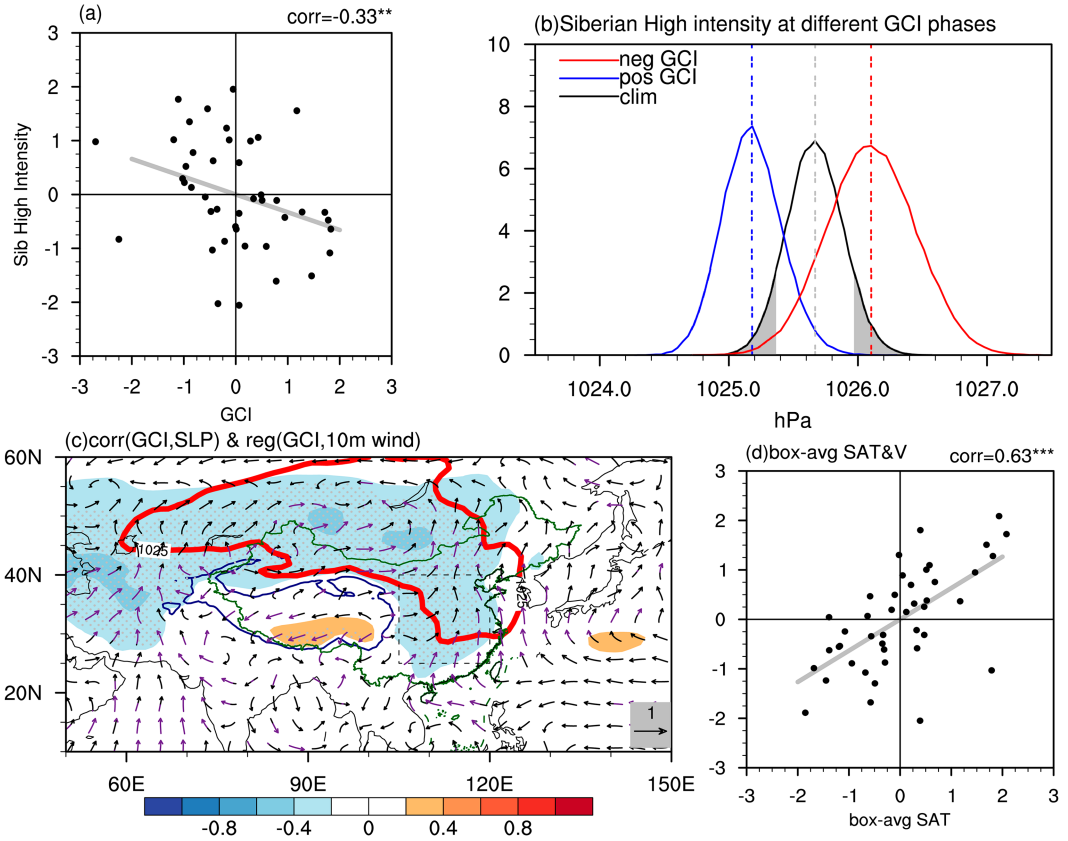

FIG. 6. (a) Normalized scatter diagram showing the GCI and Siberian High intensity. (b) The PDFs of Siberian High intensity estimated from 100 000 bootstrapped samples for the climatic mean (black curve), the positive GCI phase (blue curve), and the negative GCI phase (red curve). Vertical dashed lines show the mean value in the corresponding PDFs. Gray shading indicates the 10% tail. (c) Correlation coefficients between the GCI and SLP (shading), and regressed 10-m wind (vectors) on the GCI. The red contour with 1025 hPa outlines the Siberian High. The blue line denotes the boundary of the TP topography with an elevation of 3000 m. (d) Normalized scatter diagram showing the SAT and meridional wind averaged in the box shown in (c). The gray lines in (a) and (d) indicate the slope calculated using the least squares fitting method.

them is −0.33, passing the 0.05 significance level. Figure 6b presents PDFs of Siberian High intensity estimated from Monte Carlo bootstrap samples for the climatic mean (black curve), positive GCI phase (GCI > 0; blue curve), and negative GCI phase (GCI < 0; red curve). The resampling process was executed 100 000 times. The PDFs of Siberian High intensity for both the positive (blue curve) and the negative (red curve) phases of the GCI (Fig. 6b) are markedly separate from the climatic mean (black curve), suggesting the notable impact of the GCI on Siberian High intensity. Figure 6c shows correlation coefficients between the GCI and SLP. Negative correlation coefficients are significant over the region of the Siberian High. The results from multiple methods are consistent with each other and suggest a robust conclusion that the positive (negative) GCI anomaly favors a weakened (strengthened) Siberian High.

In the positive GCI phase (Fig. 6c), due to the weakened Siberian High, there is a tendency for anomalous southerlies, i.e., reduced northerly winds, over eastern China, signifying a weakened East Asian winter monsoon (Hu et al. 2000; Yang et al. 2002; Panagiotopoulos et al. 2005). Figure 6d presents the scatter diagram showing the meridional wind and SAT averaged within the box shown in Fig. 6c. It is evident that the SAT increases with the southerly wind, with a correlation coefficient as high as 0.63 (significant at the 0.01 level). This result indicates that a positive GCI could favor an anomalously warm winter in eastern China through the anomalous southerly (opposite to the direction of the winter monsoon flow) that is induced by a weakened Siberian High. In the negative GCI phase, the Siberian High is stronger, and an anomalous northerly flow dominates eastern China, favoring a cold SAT anomaly.

c. *Model simulation*

To support the mechanism proposed on the basis of the observational diagnostics, the 40 members of the CESM1-LE historical run for the period 1920–2005 were analyzed. Here, the first 5 and last 5 years were discarded because of the application of interannual filtering. Figure 7 shows the correlation coefficients between the GCI and SAT averaged in the box

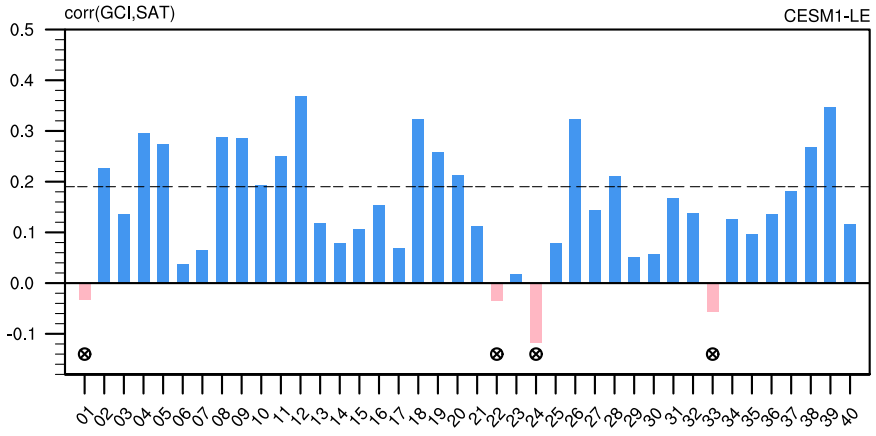

FIG. 7. Correlation coefficients between the GCI and eastern China SAT during boreal winter among the 40 CESM1-LE members. The crossed circle indicates a member that simulates a relationship between the GCI and SAT opposite to that observed. The horizontal dashed line indicates a correlation coefficient at the 0.1 significance level for the period 1920–2005.

shown in Fig. 6c, derived from the 40 CESM1-LE members. Overall, 36 of the 40 members (the exceptions are the four members marked by the crossed circles) are able to simulate the observed positive relationship between the GCI and eastern China SAT. Notably, 15 members have statistically significant correlation coefficients. However, in general, the CESM1-LE runs underestimate the observed relationship between the GCI and eastern China SAT (cf. Fig. 4a), because even the strongest correlation coefficient (found for member 12) is approximately 0.4, i.e., less than the observed value of 0.55 (Fig. 4a). Despite the low signal-to-noise ratio in the ensemble simulations, the results indicate that the observed positive relation between the GCI and the anomalously warm winter in eastern China can still be generally reproduced by the CESM1-LE simulations.

Figure 8 further presents the correlation coefficients between the GCI and the key processes of the proposed mechanism for the 40 CESM1-LE members. The crossed circles indicate members that do not simulate the observed relationships. Corresponding to the positive GCI, all members (100%) simulate the enhanced surface PV over the TP (first row), the downslope katabatic flow anomaly over the TP (second row), and the increased PV flux crossing the northern and eastern TP boundaries within the near-surface layer (third row). Over 90% of the members successfully simulate the weakened Siberian High (fourth row), resulting from the enhanced near-surface layer positive PV flux from the TP into the region of the Siberian High, the anomalous southerlies over eastern China, i.e., the weakened East Asian winter monsoon (fifth row), and, ultimately, the anomalous warm SAT in eastern China (bottom row). These results show that the mechanism derived from the reanalysis data can be well supported by numerical model simulations.

5. Summary and discussion

a. *Summary*

Using MERRA-2 and CESM1-LE model level data, this study investigated the near-surface positive PV generated by surface diabatic cooling over the TP, and its interannual impact on eastern China SAT during boreal winter. The mechanism that is proposed to be responsible for this interannual relationship is illustrated schematically in Fig. 9. We now summarize the proposed mechanism and give the main conclusions drawn from this study.

In wintertime, the vertical distribution of anomalous $\dot{\theta}$ associated with surface cooling over the TP exhibits a bottom-heavy vertical structure (left part in Fig. 9). The major cooling anomaly occurs within the shallow near-surface layer δ_0, with a thickness of approximately 88 hPa, and is strongest at the surface. This vertical gradient in the diabatic cooling rate leads to a strong positive PV anomaly confined within the shallow near-surface layer δ_0[Eq. (5)]. Further analysis suggests that the total PV generation integrated over the near-surface layer δ_0 is determined by the surface PV generation flux G_C that is thermally driven by the surface cooling [Eq. (9)].

A normalized index of interannual TP-averaged surface G_C (with the winter Niño-3.4 index linearly removed) was defined as the GCI to examine the climatic effects of the diabatic cooling–generated PV within the near-surface layer δ_0 over the TP. A positive value of the GCI indicates a positive PV generation anomaly within the near-surface layer δ_0 and a surface cooling anomaly over the TP. We found a statistically significant positive relationship between the GCI and eastern China SAT in which the positive GCI corresponds to a warm SAT anomaly over eastern China. The key processes (Fig. 9) involve the PV generation by surface diabatic cooling, PV transport by katabatic flows, and the resultant weakened Siberian High. In the positive GCI phase, the positive PV is generated within the near-surface layer δ_0 over the TP (red layer in Fig. 9). Meanwhile, the TP surface cooling anomaly behind the GCI anomaly induces the anomalous katabatic flows down the slopes of the TP (gray vectors in Fig. 9). The anomalous katabatic flows advect positive PV away from the eastern and northern sides of the TP into the region of the Siberian High. Because the Siberian High features high SLP with an anticyclonic circulation, the imported positive

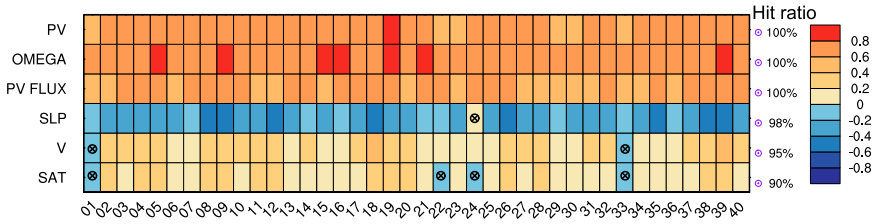

FIG. 8. Correlation coefficients for the 40 CESM1-LE members between the GCI and the key variables involved in the proposed mechanism. (first row) TP-averaged surface PV; (second row) TP-averaged omega on the lowest model level; (third row) PV flux crossing the northern and eastern TP boundaries averaged within the near-surface layer; (fourth row) Siberian High intensity; (fifth row) eastern China southerly wind; and (sixth row) eastern China SAT. The hit ratio indicates the percentage of members that can simulate the same sign of the correlation coefficient with that observed in the reanalysis. Crossed circles indicate members that simulate a relationship opposite to that observed.

surface PV weakens the intensity of the Siberian High (blue shading in Fig. 9). Finally, the weakened Siberian High is associated with a weaker East Asian winter monsoon and southerly wind anomalies over eastern China (black vectors in Fig. 9), thereby favoring an anomalously warm winter in eastern China. The negative GCI phase corresponds to the opposite situations. We used the CESM1-LE ensemble to examine the validity of the mechanism. Results suggest that 90% of the CESM1-LE ensemble members well represent the mechanism found in the reanalysis data, in which the various links are consistent in sign. Our results emphasize the importance of the diabatic cooling–generated surface PV anomaly in driving the climate anomaly over the eastern China during wintertime.

b. *Discussion*

Hoskins et al. (1985) examined the direct effect of surface diabatic cooling on the atmospheric circulation. In an idealized case, where no anomalies exist in the upper atmosphere and only surface cooling is present, their analysis using PV inversion demonstrated that a single surface cooling anomaly would directly induce anticyclonic circulation around the cooling center. This response is generally valid for the TP surface cooling, and we do see an anticyclonic circulation (Fig. 6c) around the western end of the TP where the diabatic cooling anomaly is strongest (Fig. 1c), and this noticeable anticyclonic circulation generally covers the southwestern and northwestern sides of the TP (Fig. 6c). The southerlies on the western side of the TP explain the warm SAT anomalies spanning 60°–70°E (Fig. 3a). However, this response is not apparent to the east of the TP, where there is a southerly wind (Fig. 6c) rather than the northerly wind expected from the anticyclonic circulation. This means that the direct anticyclonic response to surface cooling is not applicable over the eastern TP, and it implies that a more sophisticated mechanism of PV transport and attendant weakening of

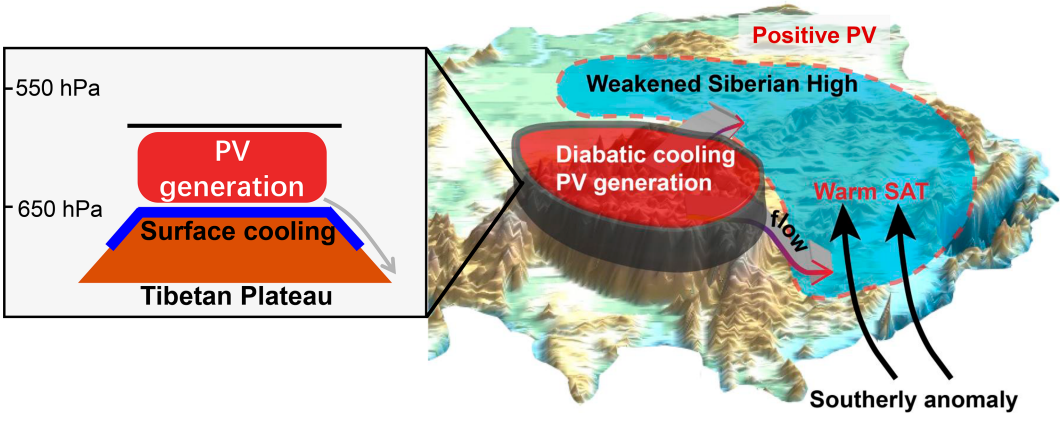

FIG. 9. Schematic showing how the diabatic cooling–generated PV anomaly within the near-surface layer influences eastern China SAT during boreal winter. The left-hand part shows details of the generation of PV due to diabatic cooling within the near-surface layer. The brown trapezoid represents the TP. The blue line represents the surface diabatic cooling anomaly. The black line indicates the top of the near-surface layer in this study. The red shading indicates the positive PV generation anomaly. The gray vector indicates the katabatic flow down the slope of the TP. In the right-hand part, the red layer over the TP indicates the diabatic cooling–generated PV within the near-surface layer. The blue shading indicates the weakened Siberian High. The red dashed line indicates the positive surface PV. The black vectors indicate the anomalous flow. The gray vectors indicate the katabatic flows down the slopes of the TP.

the Siberian High operates over the eastern TP, as proposed in this study. This is a new finding that emphasizes the importance of considering PV generation and near-surface PV transport in the climate effects of the TP. Perhaps this is because the diabatic cooling is much weaker on the east side (Fig. 1c), so that dynamical near-surface flow to the north and east advects PV off the TP is more important over the eastern part of the TP. This hypothesis will be closely examined in future work.

A katabatic flow is a common feature of the lower Antarctic atmosphere, where it is observed at low levels with a thickness of approximately 1000 m (Parish and Bromwich 1991; see their Fig. 5a). The thickness of the anomalous katabatic flow over the TP (lower panels of Figs. 5a,b) is similar to that observed over the Antarctic. Egger (1985) and Parish and Bromwich (1991) suggested that the low-level katabatic flow is an important component in establishing large-scale tropospheric motions. Over the TP, the mechanism via which the low-level katabatic flow influences the upper-level circulation anomaly that could disperse downstream along the westerly jet is an interesting topic that will be studied in the future. The spatial heterogeneity of the katabatic flow anomaly over the TP is prominent. For instance, the eastern slopes of the TP may experience stronger katabatic flow effects compared to the western slopes (Fig. 5b). This may be related to a combination of factors, such as the topography (Fig. 5b) and the interaction with the westerly wind.

The local effect of adiabatic warming that occurs as a katabatic flow moves down a slope (i.e., a foehn effect) would contribute to the positive SAT anomaly along the edges of the TP (Fig. 3a). However, for scales much larger than those considered in this study, it is important that the transport of positive PV spreads out widely. On this scale, the PV anomaly is associated with an anomalous cyclonic flow, and the southerly part of this gives rise to the widespread SAT anomalies; therefore, scale is important. The foehn effect represents a mesoscale feature local to a particular slope, whereas PV transport is important on these much larger scales.

This study has shown the influence of surface PV generation over the TP on the Siberian High intensity. Sheng et al. (2022b) found a close linkage between Rossby wave propagation and surface PV over the TP. Whether the TP can be acted as a relay station to boost the influence of Rossby wave and further exert an influence on the Siberian High is a worthy topic and will be investigated in the future.

In this paper, we have investigated the relationship between DJF-averaged anomalies in variables. However, the proposed mechanism suggests a central role for diabatic cooling which is closely related to the TP snow cover. In further work, we will investigate the possibility that TP snow cover anomalies from preceding months provide some predictive power for DJF TP snow cover and diabatic cooling, and also for the DJF Siberian High intensity and the winter surface temperatures over China.

Assuming there is a meridional wind change Δv over a zonal length scale L, and that all the change in PV goes to a change in the horizontal circulation, then we have

$$\Delta \mathrm{PV} \sim \frac{1}{\rho}\frac{\Delta v}{L}\frac{d\theta}{dz}.$$

Taking $\rho = 1.2$ kg m^{-3}, $f = 10^{-4}$ s^{-1}, $L = 10^6$ m, and $d\theta/dz = 5 \times 10^{-3}$ K m^{-1} gives that 0.2×10^{-1} PVU (1 PVU = 10^{-6} K kg^{-1} m^2 s^{-1}), which is a typical change in surface PV (Fig. 6c), corresponds to $\Delta v \sim 5$ m s^{-1}. In an inversion, on this scale, we can expect that more will go into static stability change and Δv could be down to 1–2 m s^{-1}. However, in Fig. 6c, the regressed wind over eastern China is lower than 1–2 m s^{-1}. This means that friction plays an important role in the low-level circulation anomaly. Hoskins (1991) argued that friction could be important to the large-scale circulation around the TP. In the next step, further study using data that extends to the surface (not available in MERRA-2) would be needed to dissect the relative effects of friction and heating on the circulation in this complex region.

Acknowledgments. This work was financially supported by the National Natural Science Foundation of China (42305057 and 42288101), and a fellowship founded by the China Scholarship Council (202304910130) which enabled the lead author to visit the University of Reading for a year. We thank for the technical support of the National large Scientific and Technological Infrastructure "Earth System Numerical Simulation Facility" (https://cstr.cn/31134.02.EL).

Data availability statement. All the data in this paper are publicly available from the following websites: MERRA-2 is from https://disc.gsfc.nasa.gov/datasets?keywords=%22MERRA-2%22&page=1; the Niño-3.4 index is from https://psl.noaa.gov/data/climateindices/list/; and the CESM1-LE data are from https://www.earthsystemgrid.org/dataset/ucar.cgd.ccsm4.cesmLE.html.

REFERENCES

Allaart, M. A. F., H. Kelder, and L. C. Heijboer, 1993: On the relation between ozone and potential vorticity. *Geophys. Res. Lett.*, **20**, 811–814, https://doi.org/10.1029/93GL00822.

Bowley, K. A., J. R. Gyakum, and E. H. Atallah, 2019: A new perspective toward cataloging Northern Hemisphere Rossby wave breaking on the dynamic tropopause. *Mon. Wea. Rev.*, **147**, 409–431, https://doi.org/10.1175/MWR-D-18-0131.1.

Bretherton, C. S., and C. Schär, 1993: Flux of potential vorticity substance: A simple derivation and a uniqueness property. *J. Atmos. Sci.*, **50**, 1834–1836, https://doi.org/10.1175/1520-0469(1993)050<1834:FOPVSA>2.0.CO;2.

Chen, L. X., J. P. Liu, X. J. Zhou, and P. X. Wang, 1999: Impact of uplift of Qinghai-Xizang Plateau and change of land-ocean distribution on climate over Asia (in Chinese). *Acta Meteor. Sin.*, **19**, 314–329.

Chen, Y., A. Duan, and D. Li, 2020: Atmospheric bridge connecting the Barents Sea ice and snow depth in the mid-west Tibetan Plateau. *Front. Earth Sci.*, **8**, 265, https://doi.org/10.3389/feart.2020.00265.

Danielsen, E. F., 1968: Stratospheric-tropospheric exchange based on radioactivity, ozone and potential vorticity. *J. Atmos. Sci.*,

25, 502–518, https://doi.org/10.1175/1520-0469(1968)025<0502:STEBOR>2.0.CO;2.

Ding, Y. H., Z. Y. Wang, Y. F. Song, and J. Zhang, 2008: Causes of the unprecedented freezing disaster in January 2008 and its possible association with the global warming (in Chinese). *Acta Meteor. Sin.*, **66**, 808–825.

Egger, J., 1985: Slope winds and the axisymmetric circulation over Antarctica. *J. Atmos. Sci.*, **42**, 1859–1867, https://doi.org/10.1175/1520-0469(1985)042<1859:SWATAC>2.0.CO;2.

Ertel, H., 1942: Ein neuer hydrodynamische wirbelsatz. *Meteor. Z. Braunschweig*, **59**, 33–49.

Flohn, H., 1957: Large-scale aspects of the "summer monsoon" in South and East Asia. *J. Meteor. Soc. Japan*, **35A**, 180–186.

Folkins, I., and C. Appenzeller, 1996: Ozone and potential vorticity at the subtropical tropopause break. *J. Geophys. Res.*, **101**, 18 787–18 792, https://doi.org/10.1029/96JD01711.

Gelaro, R., and Coauthors, 2017: The Modern-Era Retrospective Analysis for Research and Applications, version 2 (MERRA-2). *J. Climate*, **30**, 5419–5454, https://doi.org/10.1175/JCLI-D-16-0758.1.

Hahn, D. G., and S. Manabe, 1975: The role of mountains in the South Asian monsoon circulation. *J. Atmos. Sci.*, **32**, 1515–1541, https://doi.org/10.1175/1520-0469(1975)032<1515:TROMIT>2.0.CO;2.

He, B., G. Wu, Y. Liu, and Q. Bao, 2015: Astronomical and hydrological perspective of mountain impacts on the Asian summer monsoon. *Sci. Rep.*, **5**, 17586, https://doi.org/10.1038/srep17586.

——, Y. Liu, G. Wu, Z. Wang, and Q. Bao, 2019: The role of air–sea interactions in regulating the thermal effect of the Tibetan–Iranian Plateau on the Asian summer monsoon. *Climate Dyn.*, **52**, 4227–4245, https://doi.org/10.1007/s00382-018-4377-y.

Hoskins, B., 1997: A potential vorticity view of synoptic development. *Meteor. Appl.*, **4**, 325–334, https://doi.org/10.1017/S1350482797000716.

Hoskins, B. I., 1991: Towards a PV-θ view of the general circulation. *Tellus*, **43A**, 27–35, https://doi.org/10.3402/tellusa.v43i4.11936.

Hoskins, B. J., M. E. McIntyre, and A. W. Robertson, 1985: On the use and significance of isentropic potential vorticity maps. *Quart. J. Roy. Meteor. Soc.*, **111**, 877–946, https://doi.org/10.1256/smsqj.47001.

Hu, Z.-Z., L. Bengtsson, and K. Arpe, 2000: Impact of global warming on the Asian winter monsoon in a coupled GCM. *J. Geophys. Res.*, **105**, 4607–4624, https://doi.org/10.1029/1999JD901031.

Huang, J., and Coauthors, 2023: Global climate impacts of land-surface and atmospheric processes over the Tibetan Plateau. *Rev. Geophys.*, **61**, e2022RG000771, https://doi.org/10.1029/2022RG000771.

Kay, J. E., and Coauthors, 2015: The Community Earth System Model (CESM) large ensemble project: A community resource for studying climate change in the presence of internal climate variability. *Bull. Amer. Meteor. Soc.*, **96**, 1333–1349, https://doi.org/10.1175/BAMS-D-13-00255.1.

Lin, H., and Z. Wu, 2011: Contribution of the autumn Tibetan Plateau snow cover to seasonal prediction of North American winter temperature. *J. Climate*, **24**, 2801–2813, https://doi.org/10.1175/2010JCLI3889.1.

——, and ——, 2012: Contribution of Tibetan Plateau snow cover to the extreme winter conditions of 2009/10. *Atmos.–Ocean*, **50**, 86–94, https://doi.org/10.1080/07055900.2011.649036.

Liu, X. D., 1999: Influences of Qinghai-Xizang (Tibet) Plateau uplift on the atmospheric circulation, global climate and environment changes (in Chinese). *Plateau Meteor.*, **18**, 321–332.

Liu, Y., M. Lu, H. Yang, A. Duan, B. He, S. Yang, and G. Wu, 2020: Land–atmosphere–ocean coupling associated with the Tibetan Plateau and its climate impacts. *Natl. Sci. Rev.*, **7**, 534–552, https://doi.org/10.1093/nsr/nwaa011.

Liu, Y., L. Luan, G. Wu, and T. Ma, 2023: Impacts of the Surface Potential Vorticity Circulation over the Tibetan Plateau on the East Asian Monsoon in July. *Atmosphere*, **14**, 1038, https://doi.org/10.3390/atmos14061038.

Lu, M., S. Yang, Z. Li, B. He, S. He, and Z. Wang, 2018: Possible effect of the Tibetan Plateau on the "upstream" climate over West Asia, North Africa, South Europe and the North Atlantic. *Climate Dyn.*, **51**, 1485–1498, https://doi.org/10.1007/s00382-017-3966-5.

Ma, T., G. Wu, Y. Liu, Z. Jiang, and J. Yu, 2019: Impact of surface potential vorticity density forcing over the Tibetan Plateau on the South China extreme precipitation in January 2008. Part I: Data analysis. *J. Meteor. Res.*, **33**, 400–415, https://doi.org/10.1007/s13351-019-8604-1.

Nan, S., P. Zhao, and J. Chen, 2019: Variability of summertime Tibetan tropospheric temperature and associated precipitation anomalies over the central-eastern Sahel. *Climate Dyn.*, **52**, 1819–1835, https://doi.org/10.1007/s00382-018-4246-8.

Panagiotopoulos, F., M. Shahgedanova, A. Hannachi, and D. B. Stephenson, 2005: Observed trends and teleconnections of the Siberian high: A recently declining center of action. *J. Climate*, **18**, 1411–1422, https://doi.org/10.1175/JCLI3352.1.

Parish, T. R., and D. H. Bromwich, 1991: Continental-scale simulation of the Antarctic katabatic wind regime. *J. Climate*, **4**, 135–146, https://doi.org/10.1175/1520-0442(1991)004<0135:CSSOTA>2.0.CO;2.

Rienecker, M. M., and Coauthors, 2011: MERRA: NASA's Modern-Era Retrospective Analysis for Research and Applications. *J. Climate*, **24**, 3624–3648, https://doi.org/10.1175/JCLI-D-11-00015.1.

Rossby, C.-G., 1940: Planetary flow patterns in the atmosphere. *Quart. J. Roy. Meteor. Soc.*, **66**, 68–87, https://doi.org/10.1002/j.1477-870X.1940.tb00130.x.

Ryoo, J.-M., Y. Kaspi, D. W. Waugh, G. N. Kiladis, D. E. Waliser, E. J. Fetzer, and J. Kim, 2013: Impact of Rossby wave breaking on U.S. West Coast winter precipitation during ENSO events. *J. Climate*, **26**, 6360–6382, https://doi.org/10.1175/JCLI-D-12-00297.1.

Sandhya, M., S. Sridharan, M. I. Devi, and H. Gadhavi, 2015: Tropical upper tropospheric ozone enhancements due to potential vorticity intrusions over Indian sector. *J. Atmos. Sol.-Terr. Phys.*, **132**, 147–152, https://doi.org/10.1016/j.jastp.2015.07.014.

Sheng, C., and Coauthors, 2021: Characteristics of the potential vorticity and its budget in the surface layer over the Tibetan plateau. *Int. J. Climatol.*, **41**, 439–455, https://doi.org/10.1002/joc.6629.

——, G. Wu, B. He, Y. Liu, and T. Ma, 2022a: Linkage between cross-equatorial potential vorticity flux and surface air temperature over the mid–high latitudes of Eurasia during boreal spring. *Climate Dyn.*, **59**, 3247–3263, https://doi.org/10.1007/s00382-022-06259-4.

——, B. He, G. X. Wu, Y. Liu, S. Zhang, and P. Zhang, 2022b: Interannual Impact of the North Atlantic tripole SST mode on the surface potential vorticity over the Tibetan Plateau during

boreal summer. *J. Geophys. Res. Atmos.*, **127**, e2021JD036369, https://doi.org/10.1029/2021JD036369.

——, G. X. Wu, B. He, and Y. Liu, 2023: Aspects of potential vorticity circulation in the Northern Hemisphere: Climatology and variation. *Climate Dyn.*, **61**, 5905–5913, https://doi.org/10.1007/s00382-023-06879-4.

Son, J.-H., K.-H. Seo, and B. Wang, 2019: Dynamical control of the Tibetan Plateau on the East Asian summer monsoon. *Geophys. Res. Lett.*, **46**, 7672–7679, https://doi.org/10.1029/2019GL083104.

Sun, R., A. Duan, L. Chen, Y. Li, Z. Xie, and Y. Zhao, 2019: Interannual variability of the North Pacific mixed layer associated with the spring Tibetan Plateau thermal forcing. *J. Climate*, **32**, 3109–3130, https://doi.org/10.1175/JCLI-D-18-0577.1.

Wu, G., and Y. Cai, 1997: Vertical wind shear and down-sliding slantwise vorticity development (in Chinese). *Chin. J. Atmos. Sci.*, **21**, 273–282.

——, and Y. Zhang, 1998: Tibetan Plateau forcing and the timing of the monsoon onset over South Asia and the South China Sea. *Mon. Wea. Rev.*, **126**, 913–927, https://doi.org/10.1175/1520-0493(1998)126<0913:TPFATT>2.0.CO;2.

——, and Coauthors, 2007: The influence of mechanical and thermal forcing by the Tibetan Plateau on Asian climate. *J. Hydrometeor.*, **8**, 770–789, https://doi.org/10.1175/JHM609.1.

——, Y. Liu, B. He, Q. Bao, A. Duan, and F.-F. Jin, 2012: Thermal controls on the Asian summer monsoon. *Sci. Rep.*, **2**, 404, https://doi.org/10.1038/srep00404.

——, and Coauthors, 2015: Tibetan Plateau climate dynamics: Recent research progress and outlook. *Natl. Sci. Rev.*, **2**, 100–116, https://doi.org/10.1093/nsr/nwu045.

Wu, G. X., Y. P. Cai, and X. J. Tang, 1995: Moist potential vorticity and slantwise vorticity development (in Chinese). *Acta Meteor. Sin.*, **53**, 387–405.

——, W. J. Li, and H. Guo, 1997: Sensible heat driven air-pump over the Tibetan Plateau and its impacts on the Asian summer monsoon. *Collection in Memory of Zhao Jiuzhang*, D. Ye, Ed., Science Press, 116–126.

——, Y. M. Liu, B. He, Q. Bao, and Z. Q. Wang, 2018: Review of the impact of the Tibetan Plateau sensible heat driven air-pump on the Asian summer monsoon (in Chinese). *Chin. J. Atmos. Sci.*, **42**, 488–504.

——, and Coauthors, 2024: Potential vorticity source, potential vorticity circulation, and their weather and climate significances (in Chinese). *Chin. J. Atmos. Sci.*, **48**, 8–25, https://doi.org/10.3878/j.issn.1006-9895.2306.23319.

Xie, Y., G. Wu, Y. Liu, J. Huang, and H. Nie, 2022: A dynamic and thermodynamic coupling view of the linkages between Eurasian cooling and Arctic warming. *Climate Dyn.*, **58**, 2725–2744, https://doi.org/10.1007/s00382-021-06029-8.

——, ——, ——, ——, C. Sheng, and Y. Wu, 2023: A potential vorticity budget view of the atmospheric circulation climatology over the Tibetan Plateau. *Int. J. Climatol.*, **43**, 2031–2049, https://doi.org/10.1002/joc.7960.

Yang, H., X. Shen, J. Yao, and Q. Wen, 2020: Portraying the impact of the Tibetan Plateau on global climate. *J. Climate*, **33**, 3565–3583, https://doi.org/10.1175/JCLI-D-18-0734.1.

Yang, S., K.-M. Lau, and K.-M. Kim, 2002: Variations of the East Asian jet stream and Asian–Pacific–American winter climate anomalies. *J. Climate*, **15**, 306–325, https://doi.org/10.1175/1520-0442(2002)015<0306:VOTEAJ>2.0.CO;2.

Yeh, D. Z., S. W. Luo, and B. Z. Zhu, 1957: The wind structure and heat balance in the lower troposphere over Tibetan Plateau and its surroundings (in Chinese). *Acta Meteor. Sin.*, **28**, 108–121, https://doi.org/10.11676/qxxb1957.010.

Yu, J. J., Y. M. Liu, and G. X. Wu, 2011a: An analysis of the diabatic heating characteristic of atmosphere over the Tibetan Plateau in winter I: Climatology (in Chinese). *Acta Meteor. Sin.*, **69**, 79–88.

——, ——, and ——, 2011b: An analysis of the diabatic heating characteristic of atmosphere over the Tibetan Plateau in winter. Part II: Interannual variation (in Chinese). *Acta Meteor. Sin.*, **69**, 89–98.

Zhao, L., and Y. H. Ding, 2009: Potential vorticity analysis of cold air activities during the East Asian summer monsoon (in Chinese). *Chin. J. Atmos. Sci.*, **33**, 359–374.

Zhao, P., X. Zhou, J. Chen, G. Liu, and S. Nan, 2019: Global climate effects of summer Tibetan Plateau. *Sci. Bull.*, **64**, 1–3, https://doi.org/10.1016/j.scib.2018.11.019.

Zhou, X., P. Zhao, J. Chen, L. Chen, and W. Li, 2009: Impacts of thermodynamic processes over the Tibetan Plateau on the Northern Hemispheric climate. *Sci. China*, **52D**, 1679–1693, https://doi.org/10.1007/s11430-009-0194-9.

Zhu, H., W. Chen, T. Feng, and L. Wang, 2019: Interannual variations of Siberian High during boreal winter and its influence on East Asian temperature (in Chinese). *Plateau Meteor.*, **38**, 685–692.